Superconductivity, magnetism, and directional plasmonic modes in two-dimensional penta-bipyramid boron allotropes

L. Niu,[1] O. J. Conquest,[1,*] H. Ma,[1] C. Verdi,[1,2] and C. Stampfl[1,†]
[1]*School of Physics, The University of Sydney, Sydney NSW 2006, Australia*
[2]*School of Mathematics and Physics, The University of Queensland, Brisbane QLD 4072, Australia*

(Received 3 November 2025; accepted 8 June 2026; published 6 July 2026)

Bulk orthorhombic boron (o-B14) is an intriguing, recently predicted, three-dimensional (3D) boron allotrope. Its structure is characterized by edge-sharing pentagonal bipyramids, with diverse bond lengths. These structural motifs facilitate the formation of unusual seven-center-two-electron π bonds, predicted for the first time in 3D boron allotropes. The presence of these bonds highlights the complexity and versatility of boron chemistry under ambient conditions. Moreover, this material is predicted to be a superconductor with a critical temperature T_c of 29.1 K [Phys. Chem. Chem. Phys. **25**, 15400 (2023)]. In the present work, we explore the electronic and optical properties of bulk o-B14 and its monolayer and bilayer forms, including hydrogen termination, using first-principles calculations. These two-dimensional structures are predicted to be dynamically stable and to exhibit a remarkable variety of electronic behavior including semiconductivity with a band gap of 0.67 eV (bilayer), superconductivity with a T_c of 24.3 K (H-terminated bilayer), and magnetism (monolayer). The plasmonic and optical responses exhibit anisotropic behavior driven by the directional bonding network, as well as absorption in the visible region of the spectrum, which suggest promising opportunities for applications in advanced optoelectronic, plasmonic, and quantum devices.

DOI: 10.1103/b2q9-fytt

I. INTRODUCTION

Elemental boron possesses a unique combination of light weight, exceptional hardness, and thermal and chemical stability. Due to these properties, it has potential for high technology applications such as catalysis, sensors, energy storage, piezoelectrics, and nanodevices [1]. Boron exists in multiple allotropes with complex crystal structures arising from its electron-deficient bonding and small atomic size. The most well-characterized and stable crystalline forms are α-rhombohedral boron (α-B, 12 atoms per unit cell), β-rhombohedral boron (β-B, 105–108 atoms per unit cell) [2], and γ-orthorhombic boron (γ-B, 28 atoms per unit cell) [3]. α-B consists of B_{12} icosahedra building blocks and forms at low temperature, while β-B has the same structure, but also includes interstitial B atoms. It forms at room temperature and is the most stable structure. γ-B is also composed of B_{12} icosahedra units and forms at high pressure and temperature. The structures are predominantly characterized by covalent bonding, but the electron deficiency of boron gives rise to multicenter bonding (e.g., three-center–two-electron bonds). Additionally, boron-rich compounds exhibit promising semiconducting and thermoelectric properties, with potential use in next-generation electronics and energy-harvesting devices.

Generally, the superconducting critical temperature (T_c) of elemental superconductors is relatively low at ambient pressure, e.g., Nb has a T_c of about 9 K. Under high pressure the T_c can be significantly increased compared to at ambient pressure, but high pressure hinders experimental studies and practical applications; thus it is of high priority to explore elemental superconductors with a high T_c under low or ambient pressure. Interestingly, superconductivity with a T_c of 35 K has been reported in a three-dimensional (3D) kagome-like boron allotrope under 7 GPa on the basis of *ab initio* calculations [4], while earlier work predicts a T_c exceeding 15 K in 3D boron allotropes [5].

Boron can also form isolated clusters which exhibit many intriguing properties including fluxionality [6], that is the ability to undergo continuous structural rearrangements without breaking chemical bonds in a way that permanently alters the system. Recent studies have focused on two-dimensional (2D) forms of boron, including monolayer borophene, where many different structures have been observed as explained in recent review papers: Wang *et al.* [7] have summarized the synthesis and properties of borophene, while Mishra *et al.* [8] have reviewed the potential of borophene in various technological fields such as batteries, supercapacitors, fuel cells, and the associated synthesis techniques. Other recent reviews of borophene focus on experiment [9–12] and provide a survey of structures starting from the bulk allotropes, boron clusters, potential building blocks for 2D boron crystals, and 2D few-layered boron sheets [13]. Being a light 2D material, and also possessing good flexibility, endows it with potential applications in flexible and wearable devices, in biomedicines, and biosensors [14,15].

From the theoretical side, 2D boron has also attracted significant recent interest due to its complex electronic structure which can give rise to predicted semiconducting behavior [16]

*Contact author: catherine.stampfl@sydney.edu.au
†Contact author: oliver.conquest@sydney.edu.au

 ©2026 American Physical Society

including in twisted bilayer borophene [17], superconductivity [18,19], magnetism [20], and topological states [21–23]. Furthermore, the β_{12} sheet has been found to host gapless Dirac cones [24] and a bilayer kagome structure has been predicted to host multiple van Hove singularities [25]. Half-metallic ferromagnetism has also been reported in a 2D kagome lattice composed of a triangular arrangement of boron atoms within triangles [26].

Synthesizing borophene is notably challenging due to several intrinsic and extrinsic factors. Unlike graphene, borophene lacks a naturally occurring layered bulk counterpart, which eliminates the possibility of exfoliation-based synthesis. Its high chemical reactivity, especially with oxygen and moisture, makes it unstable under ambient conditions, requiring ultrahigh vacuum (UHV) environments for fabrication and handling. These factors collectively make the reproducible and scalable synthesis of monolayer borophene a significant materials science hurdle. To overcome the challenges of synthesizing monolayer borophene, researchers have focused on carefully controlled epitaxial growth techniques such as molecular beam epitaxy (MBE) on inert metal substrates [27]. Another study has achieved growth of β_{12} and α sheets of borophene on Ag(111) by direct evaporation of a pure boron source in an e-beam evaporator [28].

Substrates stabilize the 2D structure of borophene during growth by promoting specific polymorphs through surface templating. Maintaining UHV conditions during synthesis helps prevent oxidation and contamination. Another strategy to enhance the stability is to use hydrogen termination, which passivates the highly reactive surface boron atoms. This passivation can reduce the tendency to oxidize or react with ambient species, thereby improving chemical stability in air. Moreover, hydrogen termination can modify the electronic properties, potentially opening a band gap or altering metallic behavior, which may be advantageous for specific applications [29,30]. Large-scale synthesis of freestanding atomic sheets of borophene has been reported through a novel liquid-phase exfoliation approach, where electron microscopy confirmed the presence of the β_{12} and χ_3 phases, as well as their intermediate phases [31].

Different from the flat borophenes, a novel highly stable 2D boron structure has been recently predicted on the basis of *ab initio* calculations. It is composed of B_{12} clusters linked by single B-B bonds and is a narrow band-gap semiconductor [32]. The optical properties of 2D allotropes have also been investigated, where it has been reported that the plasmon frequencies reach the near infrared, and even visible regions, making borophene among the first materials with 2D plasmons at such high energies without doping [33].

Recently, a bulk orthorhombic boron allotrope (o-B14) with interesting properties was predicted [19]. Its structure is characterized by edge-sharing pentagonal bipyramids with varying B-B bond lengths ranging from 1.644 to 1.966 Å. These structural motifs facilitate the formation of peculiar seven-center-two-electron π bonds, which are found for the first time in 3D boron allotropes. Remarkably, this material is predicted to be a superconductor with a transition temperature of 29.1 K.

This orthorhombic o-B14 structure is a particularly promising candidate for further investigation because it introduces the pentagonal B_7 bipyramidal motif as a fundamental structural unit in crystalline boron, which differs markedly from the B_{12} icosahedral units that dominate most known boron phases. This unusual topology leads to highly delocalized multicenter bonding, including the predicted seven-center two-electron π bonds, suggesting that the electronic structure may host unconventional features such as anisotropic transport, unusual phonon behavior, and potentially strong electron-phonon coupling. Since the phase is predicted to be energetically competitive and dynamically stable at ambient pressure, *ab initio* studies of its electronic band structure, phonon spectrum, and superconducting properties, as well as for exploring how the unique bipyramidal building blocks influence the broader physics of electron-deficient boron networks, would be valuable. Moreover, the question also arises as to whether it may be stable in 2D form where the interlayer connectivity consists of just single B-B bonds.

In the present work we use density-functional theory (DFT) calculations to investigate the electronic and optical properties of bulk o-B14 and its mono- and bilayers. Hydrogen termination of the 2D structures is also considered. Interestingly, bilayer o-B14 is found to be a semiconductor with a band gap of around 0.69 eV as calculated using the HSE06 hybrid functional. The H-terminated bilayer, however, is predicted to be superconducting with a T_c of 24.3 K, while monolayer o-B14 is found to be magnetic. The optical properties reveal distinctive anisotropic behaviors and the existence of plasmons in the near to mid-infrared range for in-plane excitation as well as the ultraviolet energy range for out of plane, broadening the potential of boron for applications in optoelectronics, plasmonics, and catalysis.

The paper is organized as follows. In Sec. II the computation methods are presented, followed by the results and discussion in Sec. III. Herein we describe the electronic, superconducting, and optical properties. This is followed by the conclusion in Sec. IV.

II. COMPUTATION METHODS

The DFT calculations are performed using the Vienna *ab initio* simulation package (VASP) [34–37]. The projector augmented wave (PAW) method pseudopotentials are used to describe the electron-ion interactions [38]. The generalized gradient approximation (GGA) of Perdew-Burke-Ernzerhof (PBE) for the exchange-correlation functional [39] is employed along with the Becke-Johnson damped D3(BJ) dispersion correction to account for long-range van der Waals (vdW) interactions [40–42]. For bulk o-B14, a Γ-centered **k**-point mesh of $34\times48\times31$ is used with a plane-wave energy cutoff of 600 eV. The electronic convergence criterion is set to 10^{-6} eV and the structures are relaxed until all forces on each atom are below 0.01 eV/Å. For the 2D systems, a vacuum region of ≈22 Å is included and a **k**-point mesh of $20\times18\times1$ is used. Convergence tests show that these settings yield accurate results as shown in Figs. S1–S3 of the Supplemental Material (SM) [43].

For selected calculations we also use the screened hybrid exchange-correlation functional of Heyd, Scuseria, and Ernzerhof (HSE06), which gives more accurate band-gap energies [44–46]. All figures show results obtained using the

PBE functional unless explicitly stated otherwise. For the density-of-states (DOS) calculations for bulk o-B14, we use a Γ-centered **k**-point mesh of 20×28×18 and for the 2D systems, 20×18×1, with smearing at the Fermi level calculated with the Gaussian method and a broadening value of 0.1 eV.

The adsorption energy per atom, E_{ad}, of hydrogen atoms on the surface is calculated using Eq. (1),

$$E_{\mathrm{ad}} = (E_{\mathrm{H/B}} - E_{\mathrm{B}} - E_{\mathrm{H}})/n_{\mathrm{H}}, \tag{1}$$

where $E_{\mathrm{H/B}}$ is the total energy of the adsorption system, E_{B} is the total energy of the 2D pristine boron structure and E_{H} is the total energy of a hydrogen atom in the H_2 molecule, and n_{H} is the number of H atoms in the unit cell.

The cohesive energy per atom of the boron systems is calculated as

$$E_{\mathrm{c}} = (E_{\mathrm{B-struc}} - nE_{\mathrm{B-atom}})/n_{\mathrm{B}}, \tag{2}$$

where $E_{\mathrm{B-struc}}$ is the total energy of the boron structure of interest and $E_{\mathrm{B-atom}}$ is the total energy of a free boron atom calculated in a large supercell. n_{B} is the number of boron atoms in the unit cell of the structure.

The charge density difference, $\Delta\rho(\mathbf{r})$, for hydrogen adsorption on the surface is calculated using Eq. (3):

$$\Delta\rho(\mathbf{r}) = \rho_{\mathrm{H/B}}(\mathbf{r}) - \rho_{\mathrm{B}}(\mathbf{r}) - \rho_{\mathrm{H}}(\mathbf{r}). \tag{3}$$

The term $\rho_{\mathrm{H/B}}(\mathbf{r})$ is the total charge density of the adsorbed system and $\rho_{\mathrm{B}}(\mathbf{r})$ and $\rho_{\mathrm{H}}(\mathbf{r})$ are the total charge densities of the clean boron structure and the hydrogen atom, respectively.

The superconducting behavior of o-B14 is investigated systematically in three structural phases: bulk, monolayer, and hydrogen-terminated bilayer. Calculations are carried out using the PBE [39] formulation of the generalized gradient approximation, as provided in quantum espresso [47]. Norm-conserving pseudopotentials and a kinetic energy cutoff of 45 Ry are chosen [48] and a vacuum spacing of 15 Å is added for the 2D systems to suppress spurious periodic interactions. Monkhorst-Pack **k** meshes of 9×12×8 for the bulk, 10×10×1 for the monolayer, and 9×9×1 for the bilayer are employed to sample the Brillouin zone [49]. The phonon dispersions are calculated on **q**-point grids of 3×4×3, 5×5×1, and 3×3×1, respectively [50]. Atomic positions and lattice parameters are relaxed until residual forces are below 1×10^{-5} Ry/bohr (2.6×10^{-4} eV/Å). Maximally localized Wannier functions are constructed in Wannier90 by initializing projections on B *s* and *p* orbitals [51]. Uniform **k** meshes of 6×8×6 (bulk) and 6×6×1 (monolayer and bilayer) are used in Wannier interpolation. Superconductivity is subsequently analyzed through epw [47,52,53], which is employed to evaluate electron-phonon coupling strength and estimate Allen-Dynes transition temperatures (T_c) [54]. The superconducting properties are also obtained by solving the fully anisotropic Migdal-Eliashberg equations [54–56], as implemented in the epw code. The Morel-Anderson pseudopotential μ^* was chosen to be 0.13, consistent with the typical semiempirical range of 0.10–0.16 used in Migdal-Eliashberg calculations for light-element and *sp*-bonded superconductors [57] and with the value adopted in the literature for boron-based 2D superconductors [58]. With this choice, the calculated electron-phonon coupling strengths (λ) and T_c indicate clear dimensionality effects as discussed in Sec. III C.

For the calculation of the optical properties within VASP, in particular, the frequency-dependent dielectric function, the **k**-point meshes of (20×28×18) and (20×18×1) are found to yield converged results (cf. Fig. S4) for the bulk and 2D systems, respectively. A convergence check for the number of unoccupied bands to include in the calculation of the dielectric function was also performed. Figure S5 shows the results for bulk o-B14. It can be seen that 128 bands yield well-converged results and hereafter this value is used for all systems.

The complex frequency-dependent dielectric function, $\epsilon(\omega)$, is given by $\epsilon(\omega) = \epsilon_1(\omega) + i\epsilon_2(\omega)$, where $\epsilon_1(\omega)$ and $\epsilon_2(\omega)$ are the real and imaginary parts, respectively, and ω is the frequency in eV.

The imaginary part of the dielectric function, $\epsilon_2(\omega)$, is calculated as

$$\epsilon_2(\omega) = \mathrm{Im}\,\epsilon_{\boldsymbol{\alpha\beta}}(\omega) = \frac{4\pi^2e^2}{\Omega}\lim_{q\to0}\frac{1}{q^2}\sum_{c,v,\mathbf{k}} 2\omega_{\mathbf{k}}\delta(E_{c\mathbf{k}}-E_{v\mathbf{k}}-\omega) \times \langle u_{c\mathbf{k}+\mathbf{e}_\alpha q}|u_{v\mathbf{k}}\rangle\langle u_{v\mathbf{k}}|u_{c\mathbf{k}+\mathbf{e}_\beta q}\rangle, \tag{4}$$

where **k** is the electron wave vector, $\omega_{\mathbf{k}}$ is the **k**-point weight, q is the Bloch vector for the incident wave, and Ω is the unit cell volume [59,60]. Here v and c are the valence and conduction band indices, respectively. The $u_{v\mathbf{k}/c\mathbf{k}}$ terms are the cell periodic parts of the orbitals and $\mathbf{e}_{\boldsymbol{\alpha/\beta}}$ are the unit vectors for the three Cartesian directions. $E_{c\mathbf{k}}$ is the cth conduction band energy and $E_{v\mathbf{k}}$ is the vth valence band energy.

The real part of the dielectric function is obtained by applying the Kramers-Kronig transformation:

$$\epsilon_1(\omega) = \mathrm{Re}\,\epsilon_{\boldsymbol{\alpha\beta}}(\omega) = \delta_{\boldsymbol{\alpha\beta}} + \frac{2}{\pi}P\int_0^\infty d\omega'\frac{\omega'\epsilon_2(\omega')}{\omega'^2-\omega^2+i\eta}, \tag{5}$$

where P is the principal value and η (here $\eta = 0.1$) is the complex shift.

From the dielectric function the absorption coefficient $\alpha(\omega)$, the loss function $L(\omega)$, the refractive index $n(\omega)$, the extinction coefficient $k(\omega)$, and reflectivity $R(\omega)$ can be calculated using Eqs. (1)–(5) of the SM.

The dielectric tensor contains the combined dielectric response of the 2D material and the vacuum so that the magnitude of ϵ_1 and ϵ_2 depend linearly on the vacuum thickness [61,62]. Therefore, to obtain the intrinsic dielectric function of the structures, the calculated dielectric functions need to be renormalized. This is performed using Eqs. (6) and (7), following Ref. [63]:

$$(\epsilon_2)_{2D} = \frac{d_{SC}}{d_{2D}}(\epsilon_2)_{SC}, \tag{6}$$

$$(\epsilon_1)_{2D} = 1 + \frac{d_{SC}}{d_{2D}}[(\epsilon_1)_{SC} - 1]. \tag{7}$$

In these equations, $(\epsilon_i)_{2D}$ and $(\epsilon_i)_{SC}$ $(i = 1, 2)$ are the dielectric functions of the studied 2D structure without the influence of the vacuum region and for the whole supercell, respectively, and d_{SC} is the length of the supercell. The thickness (d_{2D}) for the monolayer, bilayer, and H-terminated bilayer is 5.897 Å, 9.412 Å, and 11.209 Å, respectively. The thickness is defined in Fig. S6 of the SM. In the literature, this correction is often ignored in studies on 2D materials, which leads to

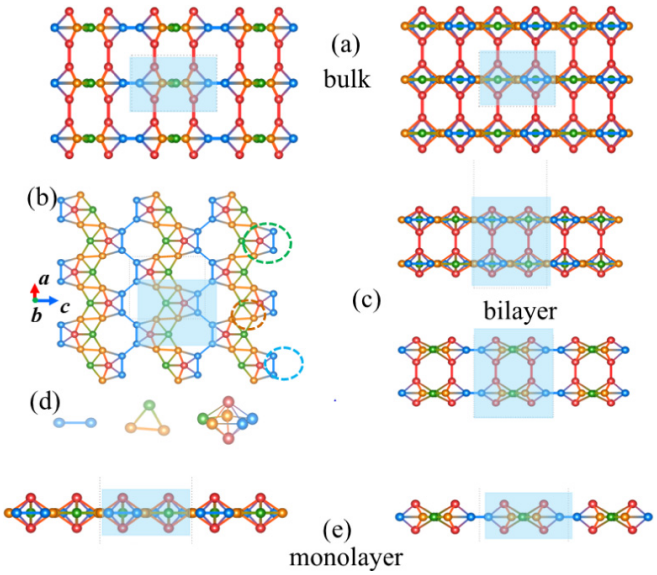

FIG. 1. Atomic structure of o-B14: (a) side views and (b) top view of the bulk structure. The unit cell is highlighted in pale blue. The B atoms are grouped into three groups, G2, G3, and G7, following Ref. [19] which relate to the two (circled in blue), three (circled in orange), and seven (circled in green) B atoms. The atoms in these groups are sketched in (d). The two side views of the bilayer (c) and monolayer (e) structure are also shown. The top view is the same as (b).

errors in the reported dielectric functions and therefore the optical properties of the 2D materials. It is noted that interband transitions presumably coexist with the plasmons forming a broad background. The coexistence of individual transitions and plasmons in the same energy range leads to a coupling of the two types of excitations and hence finite plasmon lifetimes as well as interband transitions [64].

III. RESULTS AND DISCUSSION

A. Bulk o-B14: Atomic structure and electronic properties

The structural and electronic properties of bulk o-B14 are investigated first. The atomic structure is shown in Fig. 1(a). This allotrope of boron (along with several others) has been predicted, on the basis of first-principles calculations, to be dynamically and thermodynamically stable [19]. The structural properties are listed in Table I. Following Ref. [19], the boron atoms in the unit cell are assigned to three groups as indicated by the circles in Fig. 1(b) and sketched in Fig. 1(d). This was done using the approach of solid state adaptive natural density partitioning (SSAdNDP) [65] to analyze the multicenter bonding. This method is an attempt to combine

TABLE I. Lattice constants, a, b, and c, and internal coordinates of bulk o-B14 [19].

o-B14	$a = 5.6970$ (Å)	B1 (4x) (0.52123, 0.50000, 0.63796)
	$b = 4.0479$ (Å)	B2 (4j) (0.60090, 0.50000, 0.89991)
	$c = 6.2042$ (Å)	B3 (4k) (0.75000, 0.79171, 0.72973)
	$\alpha = \beta = \gamma = 90°$	B4 (2f) (0.25000, 0.50000, 0.52367)

TABLE II. Lattice vectors a and b of the various 2D systems, interlayer B-B distance, cohesive energies (E_c), adsorption energy of hydrogen atoms on the monolayer and bilayer (E_{ad}), and electronic nature. "M" stands for metallic, "FM" for ferromagnetic, and "SC" for semiconducting.

System	a	b	Interlayer B-B (Å)	E_c	E_{ad}	Nature
Monolayer	5.700	6.314		−6.12		AFM-SC
H-Monolayer	5.694	6.134			−1.450	M
Bilayer	5.719	6.349	1.693	−6.35		SC
H-Bilayer	5.680	6.147	1.645		−1.525	M
Bulk	5.697	6.204	1.686	−6.16		M
α'-monolayer [66]				−6.00		M

the ideas of Lewis theory and aromaticity. It was found that aside from the four normal two-center–two-electron and the sixteen three-center–two-electron B-B σ bonds, there are unusual seven-center–two-electron π bonds [19].

The band structure, shown in Fig. 2 (upper), exhibits metallic behavior with three bands crossing the Fermi level. These bands include steep bands promoting high electron velocities and flat bands near the Fermi level, enhancing the density-of-states (DOS) and favoring electronic interactions. Such electronic features suggest the potential for unique transport and quantum properties. Furthermore, from the state-resolved DOS shown in Fig. 2 (lower), strong orbital hybridizations are observed between the B $2p$ orbitals within the structural units, reinforcing the stability of the bonding framework. The calculated cohesive energy of bulk o-B14 is −6.16 eV. Relative to the ground state phase of B (α-B_{12}), the total energy of o-B14 is 0.232 eV higher [19].

B. Monolayers and bilayers: Atomic and electronic structure and energetics

1. Structural properties

The atomic structure of the bilayer and monolayer is shown in Figs. 1(c) and 1(e), respectively, where a vacuum region of ∼22 Å in the direction perpendicular to the surface is included. The H-terminated bilayer structure is shown in Fig. 3(a), where the H atoms are adsorbed on top of the B atoms of the bipyramids. We also considered the hollow-bridge site for hydrogen atom adsorption, located between the two apical B atoms on each side of the layer (cf. Fig. S7). This adsorption site, however, was found to be metastable and notably less favorable (by 1.57 eV, monolayer and 2.61 eV, bilayer per H atom) than the top site.

The optimized structural parameters of the systems are given in Table II, along with the cohesive and adsorption energies and the electronic nature. Compared to bulk o-B14, it can be seen that the in-plane lattice constants of the monolayer and bilayer are slightly larger, as is the bond length of the interlayer B-B distances of the bilayer (by 0.4%). On the other hand, the in-plane lattice constants for the H-terminated monolayer and bilayer are slightly smaller compared to the bulk, as is the interlayer B-B distance (by 2.4%). The cohesive energy of the monolayer and bilayer are −6.12 eV and −6.35 eV, respectively. These values can be compared

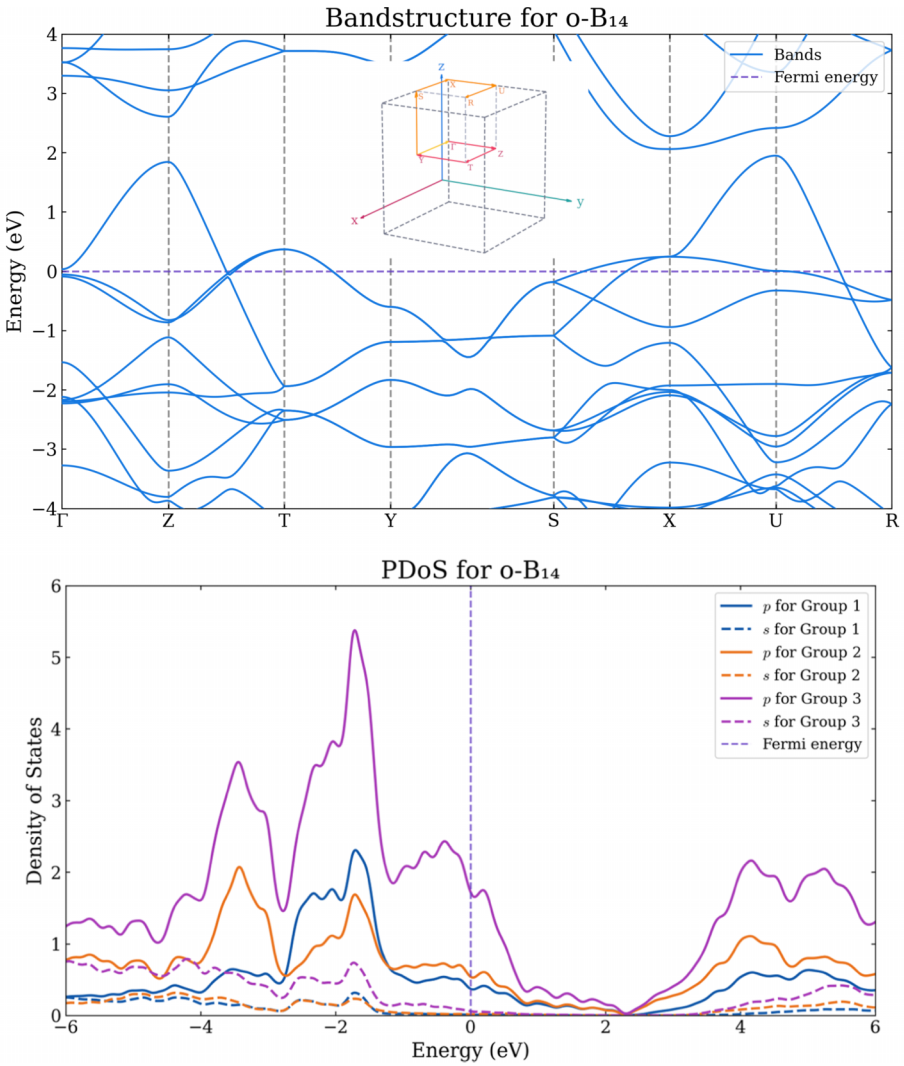

FIG. 2. Band structure of bulk o-B14 and the Brillouin zone with high symmetry **k** points labeled (upper). State-projected density of states for bulk o-B14 with the different groups of B atoms indicated by color, as defined in Fig. 1(d) (lower).

to bulk o-B14 of −6.16 eV and to that of the α' phase of borophene (−6.39 eV), which we reported in our earlier publication [66], calculated with the same approach. The adsorption energy of the hydrogen atom on the bilayer is −1.525 eV, slightly stronger than on the monolayer, which is −1.450 eV.

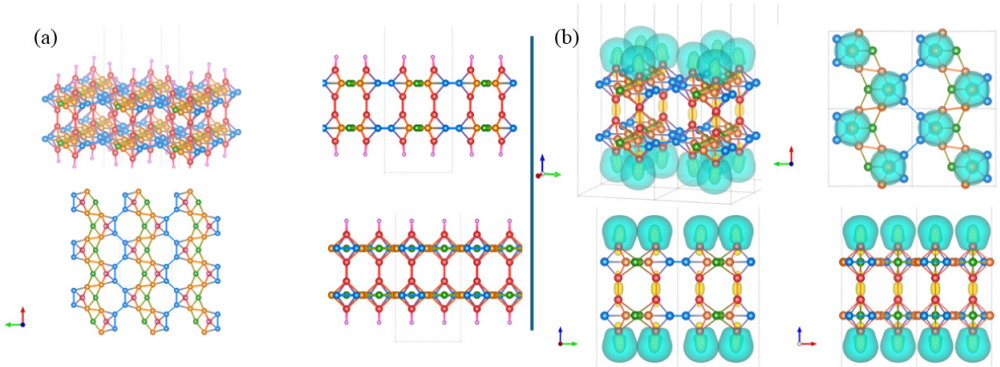

FIG. 3. Atomic structure of the hydrogen-terminated bilayer structure (a) showing a top view of the (3×3) supercell. (b) The charge density difference $[\Delta\rho(\mathbf{r})]$ showing a (2×2) supercell, calculated using Eq. (3) on adsorption of hydrogen. Regions of charge accumulation are shown in yellow and regions of charge depletion are shown in blue. The isosurface level is $1.5\times10^{-4} e\, a_0^{-3}$.

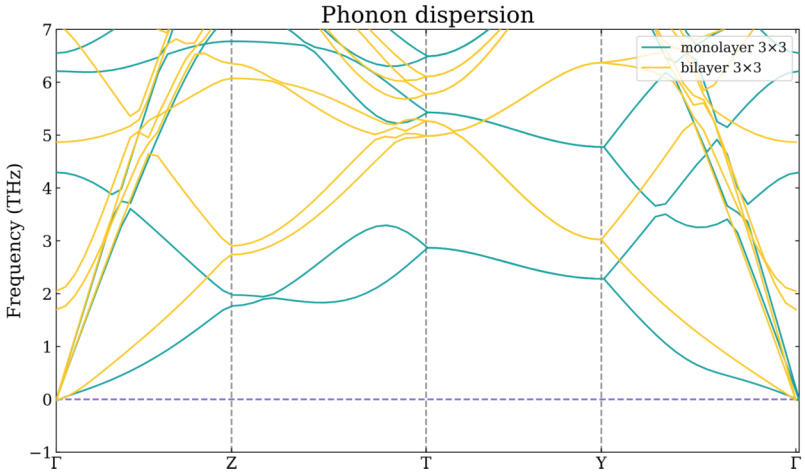

FIG. 4. Phonon dispersion curves for monolayer and bilayer o-B14, as calculated from finite differences using a (3×3) supercell.

2. Dynamic stability: Phonon dispersion

To investigate whether the monolayer and bilayer structures, both with and without hydrogen adsorption, are dynamically stable, the phonon dispersion curves are calculated. The results, obtained from finite differences using (3×3) supercells, are shown in Fig. 4 for the monolayer and bilayer. It can be seen that no imaginary frequencies are present and thus they are predicted to be dynamically stable. For the hydrogen terminated systems, we find that the H-bilayer is dynamically stable, while the H-monolayer is not. This can be seen from the presence of imaginary frequencies for the latter, but not the former, in Figs. S8 and S9 of the SM (which includes Refs. [67–69]). Based on these results, the hydrogen-terminated monolayer is not considered further. Using *ab initio* molecular dynamics (AIMD) calculations for a temperature of 400 K (using VASP), we also verified that the H-bilayer was thermodynamically stable as can be seen from Fig. S10.

3. Electronic properties

The charge density difference distribution for the adsorption of hydrogen on the surface of the bilayer is shown in Fig. 3(b). It can be seen that there is a significant depletion of electron density around the H atoms and an increase both in the interlayer B-B bonds, as well as in the p_z orbital of the uppermost bipyramid B atom directed to forming a bond with the H atom (partially hidden within the large depletion area). The increase in electron density between the interlayer B-B bond is consistent with the slightly smaller distance compared to without H adsorption.

The band structure of the monolayer is shown in Fig. 5 as calculated using the HSE06 functional with spin polarization. It is found that the antiferromagnetic (AFM) configuration (Fig. 5, center) is more favourable than the ferromagnetic (FM) configuration [Fig. 5, upper and Fig. S11 (PBE)] by 0.02 eV. A small band gap of 0.105 eV opens up in the AFM case.In the nonmagnetic state, the system is metallic and exhibits a high DOS at the Fermi level which is related to flat bands throughout the Brillouin zone and particularly along the T-Y direction (Figs. S12 and S13). Since a large DOS at the Fermi level often suggests that a material is prone to

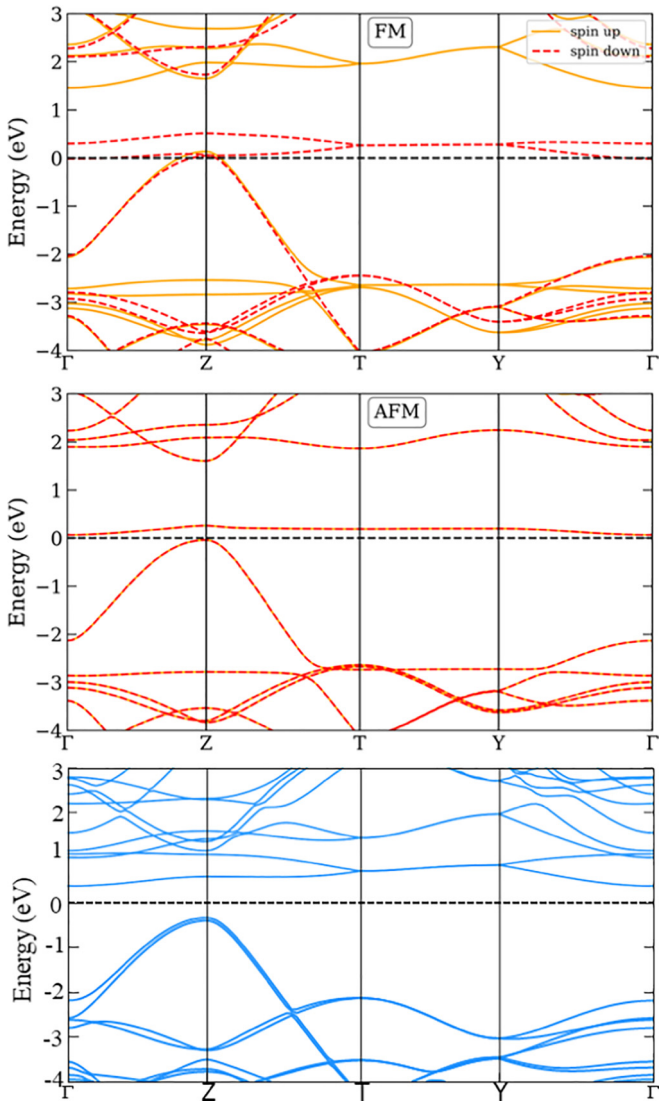

FIG. 5. Spin-polarized band structure of the monolayer as calculated using the HSE06 functional: FM, upper and AFM, center. Band structure of the bilayer calculated using the HSE06 functional (lower). The Fermi energy is the energy zero and, for the semiconducting systems, the energy zero is in the middle of the band gap.

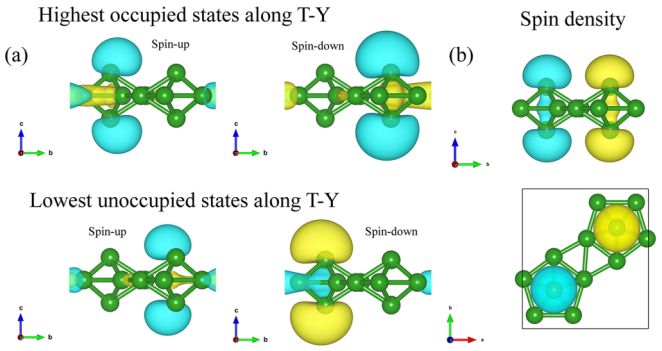

FIG. 6. (a) Highest occupied and lowest unoccupied spin-up and spin-down states of the monolayer in the AFM state at a **k** point midway along the high symmetry T-Y direction (isosurface is $1\times10^{-7}e/\text{Å}^3$). (b) The spin density of the monolayer. The isosurface is $0.005e/\text{Å}^3$.

undergo transitions to more stable ground states, such as forming superconductors, ferromagnets, or experiencing structural distortions like the Jahn-Teller effect (cf. Fig. S14), we tested all these aspects. As mentioned above, it is found that the structure is magnetic, with a magnetic moment of 0.262 μ_B on each apical B atom. For the FM case, fixed-spin calculations (cf. Fig. S15) show a total magnetic moment of the unit cell of around $2\mu_B$. The DOS of the FM structure clearly shows the significant spin splitting (spin up and spin down) of the states related to the apical B atoms (Fig. S16, upper). The DOS for the AFM ordering is shown in Fig. S16 (lower).

For the AFM case, the spatial distribution of the wave function of the highest occupied and lowest unoccupied states at a **k**-point midway along the high-symmetry line T-Y in the BZ is shown in Fig. 6(a), along with the total spin density, shown in Fig. 6(b). It is apparent that the apical B atoms of the bipyramid are responsible for the magnetic behavior of the system where they have a magnitude $0.262\mu_B$. The analogous result for the FM ordering is shown in Fig. S17. The energetic preference for AFM ordering over FM ordering can be understood in terms of the competition between electron hopping and exchange interactions. In the AFM configuration, virtual hopping between neighboring magnetic sites is enhanced because electrons can delocalize onto oppositely aligned spins without violating the Pauli exclusion principle, leading to a greater kinetic-energy lowering. In contrast, FM alignment restricts such virtual hopping processes and reduces the associated kinetic-energy gain, rendering the AFM state energetically more favorable.

The band structure of the bilayer is shown in Fig. 5 (lower), as calculated using the HSE06 functional. The bilayer is an indirect semiconductor with a band gap of 0.67 eV, where the valence band maximum (VBM) is at the Z point and the conduction band minimum at the Γ point. Using the PBE results in a semimetal. On terminating the bilayer structure with hydrogen, the band structure changes dramatically. Specifically, it can be seen from Fig. 7 that the system is now metallic and bears some resemblance to that of the bulk band structure.

C. Superconducting properties of o-B14

The (conventional) superconducting properties of bulk o-B14, the monolayer, and H-terminated bilayer are investigated. The bilayer is not considered due to its semiconducting nature. We first confirm that the atomic relaxation obtained using Quantum Espresso (QE) yields very similar results to those obtained by VASP, namely, we obtain lattice constants a, b: QE 5.66, 6.12 Å; VASP 5.68, 6.14 Å; interlayer distance: QE 4.13 Å; VASP 4.11 Å; H-B distance: 1.19 Å, in both cases. For the bulk phase, an electron phonon coupling strength of $\lambda = 0.931$ is obtained, corresponding to an estimated Allan-Dynes superconducting temperature of $T_c = 28.2$ K, consistent with the prior report of 29.1 K [19]. The hydrogen-terminated bilayer exhibits a slightly higher coupling strength ($\lambda = 1.01$) but a lower $T_c = 18.5$ K, which may be attributed to the phonon softening effects arising at higher electron phonon coupling strengths [70–72]. The monolayer phase yields $\lambda = 0.05$ and a negligible T_c, indicating the absence of significant phonon-mediated superconductivity.

From the anisotropic Migdal-Eliashberg equations, analysis of the superconducting gap evolution further supports these findings: the bulk gap is observed close to around $T_c = 31.3$ K [Fig. 8(a)] and the bilayer gap around $T_c = 24.3$ K [Fig. 8(b)].

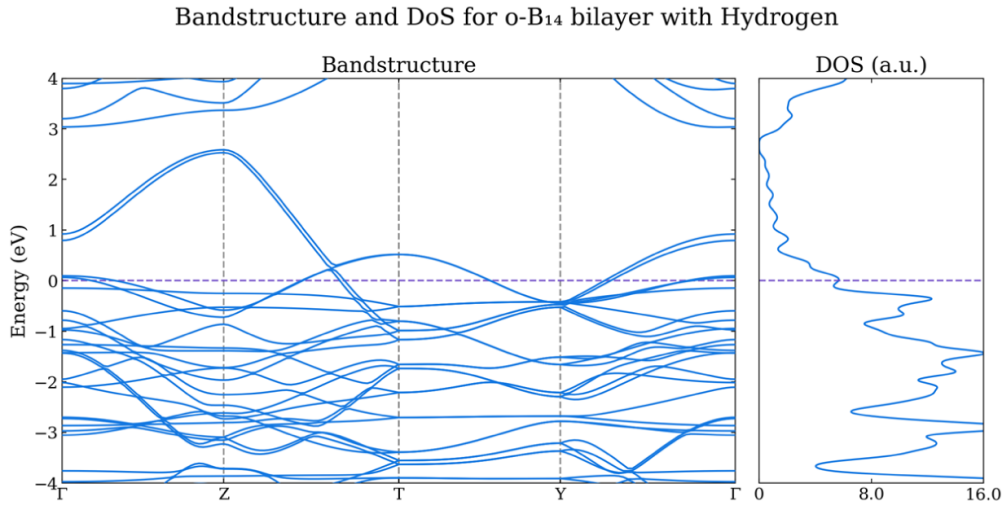

FIG. 7. Band structure and total density of states for the bilayer with hydrogen termination.

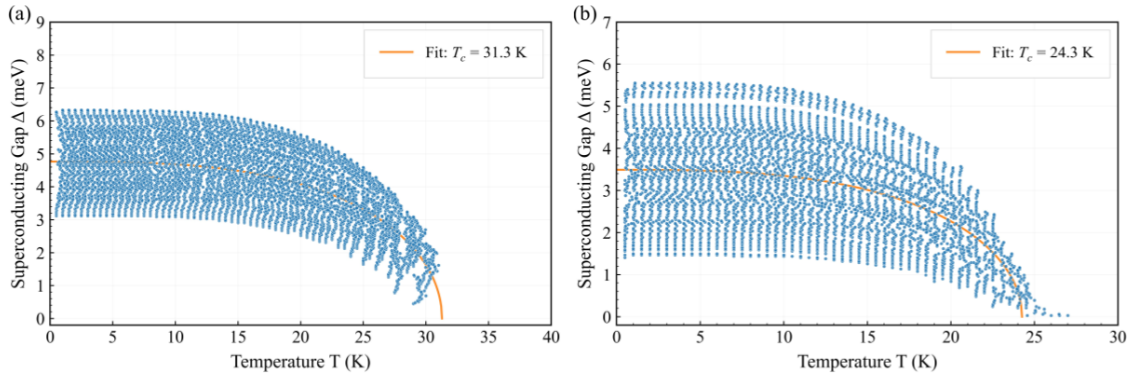

FIG. 8. Superconducting gap versus temperature for (a) bulk o-B14 and (b) hydrogen-terminated bilayer o-B14.

Overall, these results suggest that o-B14 is unlikely to possess conventional superconductivity in the monolayer phase owing to the extremely weak electron phonon interactions, whereas the bulk and hydrogen-terminated bilayer possess credible phonon-mediated superconducting states corresponding to transition temperatures ranging between 20 and 30 K.

D. Optical properties

The optical properties are now considered. In particular, the real (ϵ_1) and imaginary part (ϵ_2) of the dielectric function are calculated and from them the other optical properties are determined [cf. Eqs. (1)–(5) of the SM]. The imaginary part, ϵ_2, is a measure of light absorption as a consequence of neutral and plasmonic charge excitations and ϵ_1 is a measure of the strength of the dynamical screening effects arising from charge excitations. Metallic character is indicated by a negative value of $\epsilon_1(\omega)$ for the corresponding ranges of the electromagnetic spectrum. For a plasmon resonance, $\epsilon_1(\omega)$ must typically cross from a negative value to positive with increasing energy. This behavior indicates a restoring force becoming insufficient to fully screen the external field, a condition where plasma oscillations (plasmons) can be excited. In metals, at low frequencies, $\epsilon_1(\omega)$ is usually negative, indicating a metallic (screening) response. As it increases, the ability to screen weakens and $\epsilon_1(\omega)$ increases. A plasmon resonance is reached when $\epsilon_1(\omega) = 0$ and when $\epsilon_2(\omega)$ is close to zero, indicating the onset of collective charge oscillations. The plasmon will then be optically active, i.e., it strongly couples to light or other external probes and appears as a distinct peak in spectra [e.g., reflectivity, electron energy loss spectroscopy (EELS), and absorption].

Figure 9 shows the real and imaginary parts of the dielectric function for all the structures considered for the *xx*, *yy* (in-plane), and *zz* (out-of-plane) components. It can be seen that each component of the dielectric function is different, indicating that the response of the structures to light is highly dependent on the polarization direction of incoming light. That is, the systems exhibit anisotropy, leading to polarization-dependent optical properties and directionally selective light-matter interactions.

For photon energies less than around 2.0 eV, the *xx* and *yy* components differ for the bulk and hydrogen-terminated bilayer in that ϵ_1 for the *xx* component is negative in part of this region while the *yy* is not. It also can be seen that, for some range of energies the monolayer, hydrogen terminated bilayer, and bulk system behave as indefinite media, for which in-plane and out-of-plane ϵ_1 are of opposite sign, namely in the region below 2.0 eV for the former two systems and between 6.0 eV and 10.0 eV for the latter, signaling directional plasmonic modes.

The real part of the dielectric function for the *xx* component, shows that there is a plasmon for the bulk, monolayer, and the hydrogen terminated bilayer, in the region between 0.5 and 1.5 eV, where the imaginary part is correspondingly very low. For the monolayer, this plasmon persists in the *yy* direction and is even more pronounced, while for the bulk and hydrogen-terminated bilayer it is not present. Interestingly, in the out-of-plane *zz* direction, the presence of plasmons as indicated by the negative values of $\epsilon_1(\omega)$ is seen for the H-terminated bilayer, monolayer, and the bilayer at around 1.5 eV, 3.6 eV and 6.0 eV, and 5.0 eV, respectively, which correspond to the significant peaks in the energy loss spectrum in Fig. 10 (lower).

Peaks in the imaginary part of the dielectric function signal strong absorption due to electronic transitions, typically interband excitations. The energy, width, and intensity reflect the band structure and optical activity. In the present case, except for the bilayer, characteristic metallic behavior is observed, namely, a large value at low energies, due to the intraband (Drude) absorption from free electrons. The bilayer, on the other hand, is small until interband transitions begin, consistent with its semiconducting nature. The dielectric tensor characterizes how the polarization of the material changes in response to an applied electric field. For an incident photon, the tensor components represent the response of the material to the electric field component of the photon along different directions, e.g., the elements ϵ_{yx} and ϵ_{xy} describe the response to an electric field applied along the *y* direction, resulting in polarization along the *x* direction and vice versa. A nonsymmetric dielectric tensor, i.e., $\epsilon_{yx} \neq \epsilon_{xy}$, implies time-reversal symmetry is broken and can lead to Faraday rotation (the rotation of light polarization during propagation), circular dichroism, and nonreciprocal light propagation. This results in light behaving differently depending on the direction it travels through a material. For all systems studied here, however, the off-diagonal components of the dielectric tensor are zero.

In order to further explore the optical properties of the o-B14 based structures, the absorption coefficient, loss function, reflectivity, refractive index, and extinction coefficient are

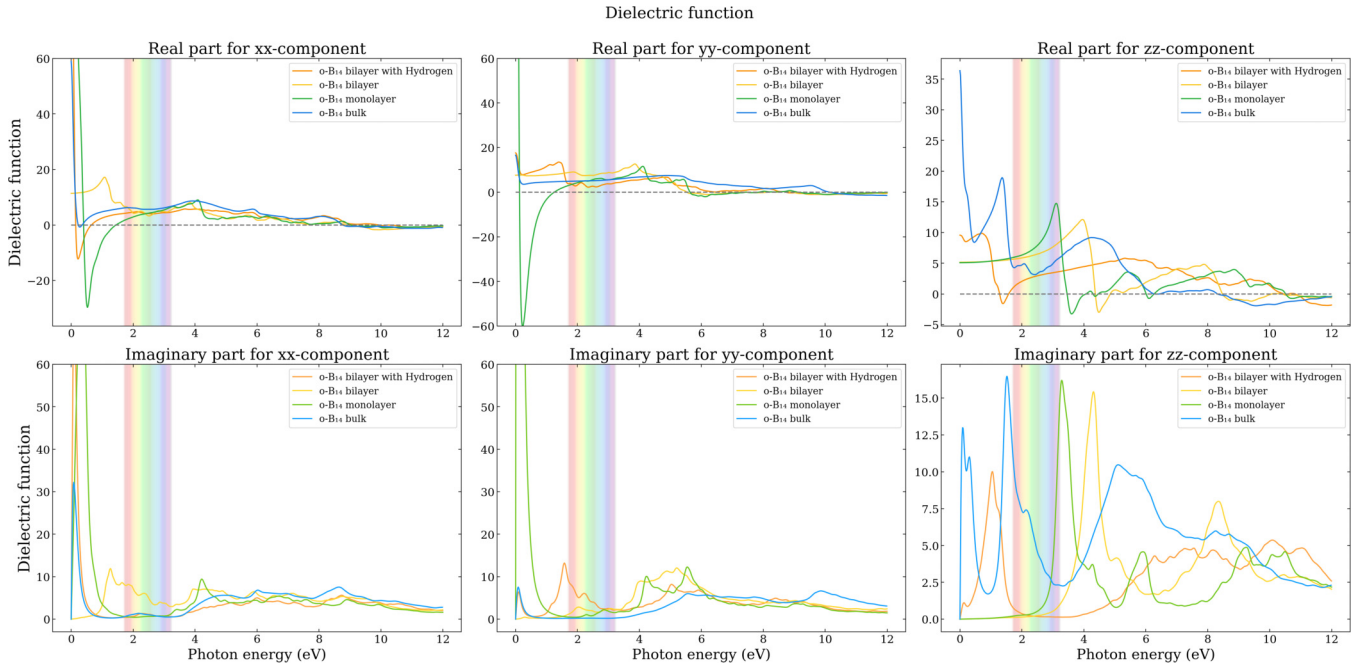

FIG. 9. Real and imaginary parts of the dielectric function for the bulk and 2D o-B14 structures for the *xx*, *yy*, and *zz* directions.

calculated. Figure 10 shows the absorbance and loss function for the various structures. The absorption coefficient is directly proportional to the imaginary part of the dielectric function, where the absorbance threshold corresponds to where $\epsilon_2(\omega)$ shows its first peak. For all but bilayer o-B14, the threshold is close to zero, corresponding to the metallic nature. With regard to the absorption coefficient, in the visible region of the spectrum (1.7–3.3 eV) it can be seen that for the *xx*, *yy*, and *zz* components, the bilayer, H-bilayer, and bulk systems have significantly the greatest value of absorption coefficient, respectively. The monolayer, on the other hand, exhibits strong absorption in the near-infrared and ultraviolet. This value of around 0.005 Å (or 5×10^{-5} cm^{-1}) is similar to that calculated for bulk silicon [73] and notably larger than that reported for bilayer silicon as calculated by the same approach [73].

The loss function in Fig. 10 (lower) exhibits several sharp peaks. For the *xx* component, plasmon excitations can be seen

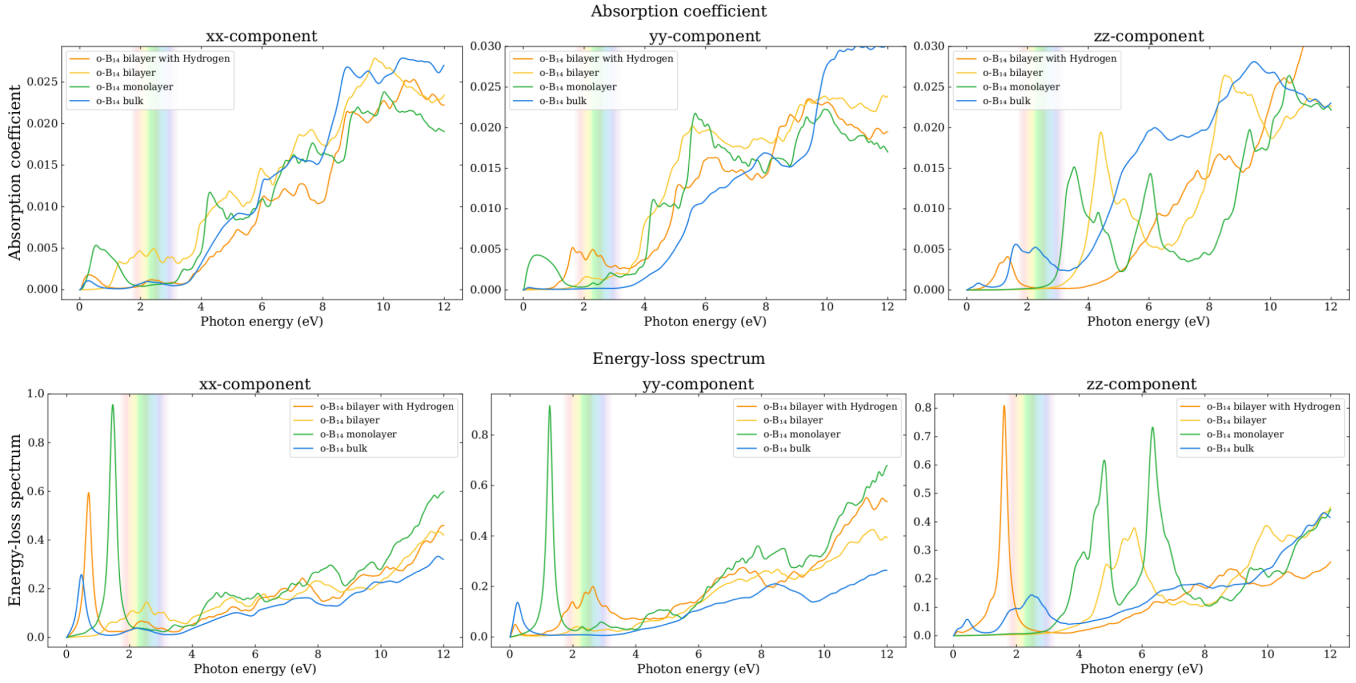

FIG. 10. Absorption (Å^{-1}) and energy loss for the bulk and 2D o-B14 structures for the in-plane (*xx*, *yy*) and out-of-plane (*zz*) directions.

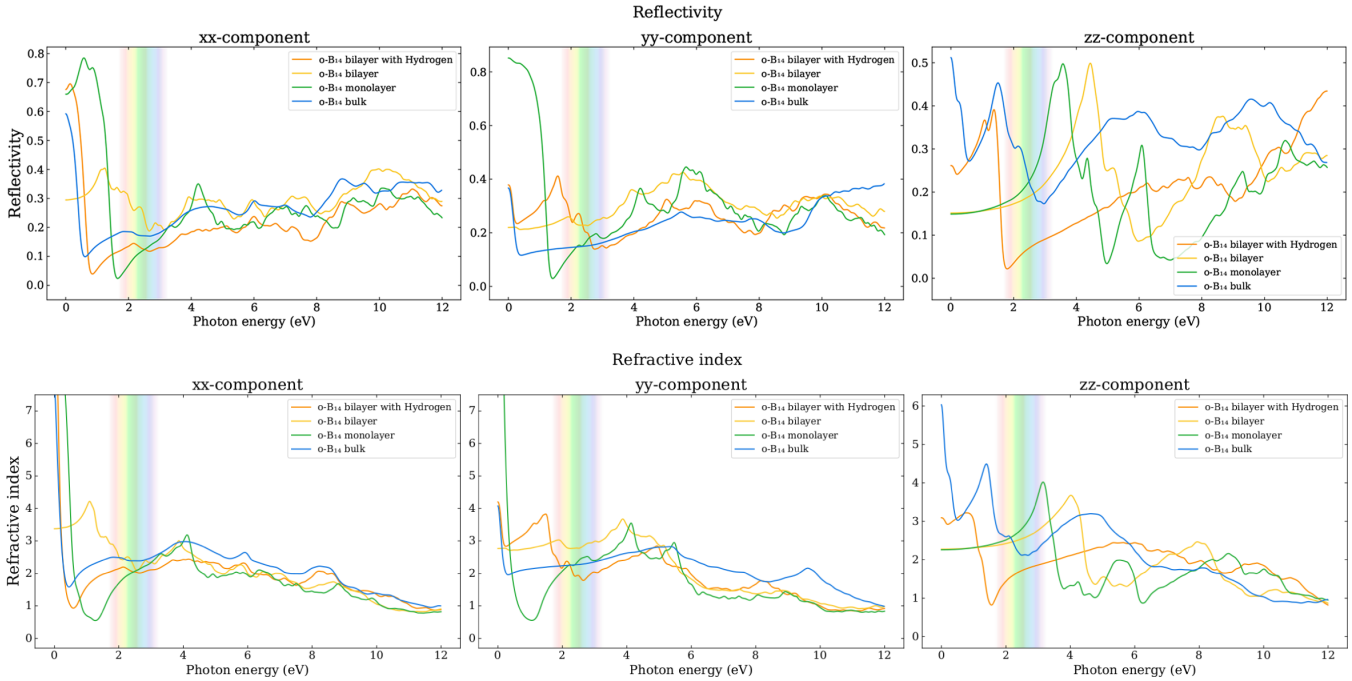

FIG. 11. Reflectivity and refractive index as a function of energy for the bulk and 2D o-B14 structures for the in-plane (*xx*, *yy*) and out-of-plane (*zz*) directions.

below 2.0 eV for the bulk, H-bilayer, and monolayer, while for the *yy* component only the monolayer shows a strong excitation in this energy range. In the out-of-plane direction, there is a strong peak for the H-bilayer below 2 eV, while the monolayer exhibits two strong features at around 4.0 eV and 6.0 eV corresponding to the above-mentioned plasmons. The bilayer also has a strong feature at about 5.0 eV.

In Fig. 11, the reflectivity and refractive index are shown. The reflectivity features directly reflect the electronic structure, where the drops in it correlate with the edges of the above-discussed plasmons. It can be seen that the trends in refractive index are similar to ϵ_1, which indicates that the effect of the real part of the dielectric function on the refractive index plays the leading role. The refractive index determines how much the path of light is bent, or refracted, when entering a material. Most transparent materials have refractive indices between one and two for visible light. The absolute refractive index of an optical medium is defined as the ratio of the speed of light in vacuum and the phase velocity (speed at which the crests of the wave move) of light in a material. It is possible for the phase velocity to travel faster than the speed of light in vacuum so the refractive index can be less than one. Near the plasmon resonance in 2D materials, the refractive index can drop below one due to the strong interaction between light and the plasmonic oscillations. Metals can have a high refractive index at low photon energies due to strong absorption and, as the energy increases, the refractive index drops to values between one and two, particularly near, or beyond, interband transitions and the plasma edge. This change reflects how the material transitions from strongly reflective/absorptive (not transmitting light) to partially transparent or weakly reflective at higher energies.

It can be seen from Fig. 11 (lower) that the refractive index for in-plane polarization is close to and less than one for energies in the range of ∼0.5–1.5 eV for the monolayer. For out of plane, this occurs at energies around 1.5 eV (H-bilayer), 3.6, and 6 eV (monolayer) and around 4.8 eV (bilayer). This means that, in these ranges of the electromagnetic spectrum, the structures are highly transparent and it is in the region of where the plasmons occur. The extinction coefficient (imaginary part of the complex refractive index) provides direct insight into how strongly a material absorbs light at different photon energies. It is noticeable that the extinction coefficient (shown in Fig. S18) exhibits sharp dips/peaks near the above-mentioned plasmon resonances. Near a plasmon resonance, especially in surface plasmon polaritons or localized surface plasmons, the dielectric function changes rapidly, both in the real and imaginary parts, and this affects the extinction coefficient causing sharp features, including dips/peaks, near resonances. That is, these dips/peaks may indicate a frequency where the energy is lost not via absorption, but resonant energy transfer to the plasmon. Specifically, these dips/peaks are seen around (i) 0.5 eV and 1.3 eV (*xx*), 1.0 eV and 6.0 eV (*yy*), and 3.5 eV and 6.0 eV (*zz*) for the monolayer, (ii) 2.0 eV (*yy*) and 4.5 eV and 9.0 eV (*zz*) for the bilayer, (iii) 0.5 eV (*xx*), 2.0 eV and 6.0 eV (*yy*), and 1.5 eV (*zz*) for the H-bilayer, and (iv) 0.5 eV and 8.8 eV (*xx*), 0.2 eV and 10 eV (*yy*), and 0.5 eV, 2.0 eV and in the range 6.3–8.3 eV (*zz*) for the bulk. Overall, the plasmonic and optical properties of the o-B14 structures display interesting anisotropic effects that could offer opportunities for advanced optoelectronic, plasmonic, and quantum devices.

IV. CONCLUSION

In the present work, the electronic, optical, and superconducting properties of novel o-B14 based structures were investigated on the basis of density functional theory calcu-

lations. Namely, we consider the three-dimensional bulk as well as the 2D monolayer, bilayer, and hydrogen terminated bilayer. The cohesive energy of the monolayer is slightly less than that of the bulk (by 0.04 eV/atom), while the bilayer is notably more stable than the bulk (by 0.19 eV). The 2D allotropes of o-B14 reveal complex properties including semiconductivity in the bilayer (band gap of 0.67 eV), magnetism in the monolayer, and superconductivity in the hydrogen-terminated bilayer (with a T_c of 24.3 K). The calculated optical properties show absorption in the visible region of the spectrum for the bilayer, hydrogen terminated bilayer, and bulk in the *xx*, *yy*, and *zz* directions, respectively. All the metallic systems display plasmons in the in-plane direction for energies below around 1.5 eV, while plasmons are present for all systems in the out-of-plane direction. Interestingly, the monolayer and bulk systems behave as indefinite media, for which the real part of the dielectric function in the in-plane and out-of-plane directions are of opposite sign, namely in the region below 2.0 eV for the former and between 6.0 eV and 10.0 eV for the latter, indicating directional plasmonic modes. All together, these complex optical, electronic, and superconducting properties emphasize the rich physics of boron materials which could hold potential for future high technologies.

ACKNOWLEDGMENTS

This research was undertaken with the assistance of resources from the National Computational Infrastructure (NCI Australia), an NCRIS enabled capability supported by the Australian Government. C.V. acknowledges financial support from the Australian Research Council (Grant No. DE220101147) and C.S. acknowledges financial support from the Australian Research Council (Grant No. FL230100176).

DATA AVAILABILITY

The original data presented in this study is openly available [74].

[1] P. Ranjan, R. Tiwari, R. Khan, A. Singh, and L. S. Banjara, Properties of Boron manocrystals, borophene, and its polymorphs, in *2D Boron Nanosheets: Synthesis and Applications* (Springer, Berlin, 2024), p. 83.

[2] M. Widom and M. Mihalkovič, Symmetry-broken crystal structure of elemental boron at low temperature, Phys. Rev. B **77**, 064113 (2008).

[3] Q. An, K. M. Reddy, K. Y. Xie, K. J. Hemker, and W. A. Goddard, New ground-state crystal structure of elemental boron, Phys. Rev. Lett. **117**, 085501 (2016).

[4] Z. Ouyang, M. Gao, and Z.-Y. Lu, Superconductivity in a three-dimensional kagome-like boron allotrope, Phys. Rev. B **111**, 134518 (2025).

[5] S. Zhang, X. Du, J. Lin, A. Bergara, X. Chen, X. Liu, X. Zhang, and G. Yang, Superconducting boron allotropes, Phys. Rev. B **101**, 174507 (2020).

[6] S. Pan, J. Barroso, S. Jalife, T. Heine, K. R. Asmis, and G. Merino, Fluxional boron clusters: From theory to reality, Acc. Chem. Res. **52**, 2732 (2019).

[7] K. Wang, S. Choyal, J. F. Schultz, J. McKenzie, L. Li, X. Liu, and N. Jiang, Borophene: Synthesis, chemistry, and electronic properties, ChemPlusChem **89**, e202400333 (2024).

[8] R. K. Mishra, J. Sarkar, K. Verma, I. Chianella, S. Goel, and H. Y. Nezhad, Borophene: A 2D wonder shaping the future of nanotechnology and materials science, Nano Mater. Sci. **7**, 198 (2025).

[9] S. Mohanty, D. Panda, A. Dash, S. S. Kumar, R. R. Padhi, S. Guhathakurata, and S. Mallik, A review on borophene: A potential gas-capture material, J. Electron. Mater. **52**, 4434 (2023).

[10] R. Yang and M. Sun, Borophenes: Monolayer, bilayer and heterostructures, J. Mater. Chem. C **11**, 6834 (2023).

[11] P. Kumar, G. Singh, R. Bahadur, Z. Li, X. Zhang, C. I. Sathish, M. R. Benzigar, T. Kim, A. Tran, N. T. Padmanabhan, S. Radhakrishnan, *et al.*, The rise of borophene, Prog. Mater. Sci. **146**, 101331 (2024).

[12] Z. Xie, X. Meng, X. Li, W. Liang, W. Huang, K. Chen, J. Chen, C. Xing, M. Qiu, B. Zhang, *et al.*, Two-dimensional borophene: Properties, fabrication, and promising applications, Research **2020**, 2624617 (2020).

[13] X. Sun, X. Liu, J. Yin, J. Yu, Y. Li, Y. Hang, X. Zhou, M. Yu, J. Li, G. Tai, *et al.*, Two-dimensional boron crystals: Structural stability, tunable properties, fabrications and applications, Adv. Funct. Mater. **27**, 1603300 (2017).

[14] S. M. Mozvashi, M. A. Mohebpour, S. I. Vishkayi, and M. B. Tagani, Mechanical strength and flexibility in $\alpha\prime$-4h borophene, Sci. Rep. **11**, 7547 (2021).

[15] Z. Zhang, Y. Yang, E. S. Penev, and B. I. Yakobson, Elasticity, flexibility, and ideal strength of borophenes, Adv. Funct. Mater. **27**, 1605059 (2017).

[16] A. H. Qureshi, Y. Sun, L. Wang, Y. Wang, X. Yao, and X. Zhang, Bilayer borophene allotropes: Structural stabilities and electronic properties, ACS Appl. Nano Mater. **7**, 15685 (2024).

[17] X. Jin, X. Wang, R. Wu, Y. Gao, Y. Yan, and F. Xuan, Tuning band gaps in twisted bilayer borophene, J. Phys. Chem. C **126**, 17769 (2022).

[18] M. Gao, Q.-Z. Li, X.-W. Yan, and J. Wang, Prediction of phonon-mediated superconductivity in borophene, Phys. Rev. B **95**, 024505 (2017).

[19] S. Han, Y. Liu, C. Wang, W. Yi, X. Chen, Y. Zhang, and X. Liu, Superconducting boron allotrope featuring pentagonal bipyramid at ambient pressure, Phys. Chem. Chem. Phys. **25**, 15400 (2023).

[20] M.-H. Zhu, X.-J. Weng, G. Gao, S. Dong, L.-F. Lin, W.-H. Wang, Q. Zhu, A. R. Oganov, X. Dong, Y. Tian, *et al.*, Magnetic borophenes from an evolutionary search, Phys. Rev. B **99**, 205412 (2019).

[21] L. Wang, A. H. Qureshi, Y. Sun, X. Xu, X. Yao, A.-L. He, Y. Zhou, and X. Zhang, Second-order topological insulator in bilayer borophene, Phys. Rev. B **111**, 035113 (2025).

[22] S. Rakshit and N. G. Szwacki, Exploring the structure and properties of-sheet based bilayer borophenes, Sci. Rep. **15**, 349 (2025).

[23] A. Wang, L. Shen, M. Zhao, X. Zhang, T. He, W. Li, Y. Feng, and H. Liu, Serendipity of a topological nontrivial band gap in

the 2D borophene subunit lattice with broken mirror symmetry, Phys. Chem. Chem. Phys. **21**, 22526 (2019).
[24] B. Feng, O. Sugino, R.-Y. Liu, J. Zhang, R. Yukawa, M. Kawamura, T. Iimori, H. Kim, Y. Hasegawa, H. Li, *et al.*, Dirac fermions in borophene, Phys. Rev. Lett. **118**, 096401 (2017).
[25] Q. Gao, Q. Yan, Z. Hu, and L. Chen, Bilayer kagome borophene with multiple Van Hove singularities, Adv. Sci. **11**, 2305059 (2024).
[26] S. Kim, W. H. Han, I.-H. Lee, and K. J. Chang, Boron triangular kagome lattice with half-metallic ferromagnetism, Sci. Rep. **7**, 7279 (2017).
[27] C. Chen, H. Lv, P. Zhang, Z. Zhuo, Y. Wang, C. Ma, W. Li, X. Wang, B. Feng, P. Cheng, *et al.*, Synthesis of bilayer borophene, Nat. Chem. **14**, 25 (2022).
[28] Q. Zhong, J. Zhang, P. Cheng, B. Feng, W. Li, S. Sheng, H. Li, S. Meng, L. Chen, and K. Wu, Metastable phases of 2D boron sheets on Ag (1 1 1), J. Phys.: Condens. Matter **29**, 095002 (2017).
[29] C. Hou, G. Tai, J. Hao, L. Sheng, B. Liu, and Z. Wu, Ultrastable crystalline semiconducting hydrogenated borophene, Angew. Chem. Int. Ed. **59**, 10819 (2020).
[30] Q. Li, V. S. C. Kolluru, M. S. Rahn, E. Schwenker, S. Li, R. G. Hennig, P. Darancet, M. K. Y. Chan, and M. C. Hersam, Synthesis of borophane polymorphs through hydrogenation of borophene, Science **371**, 1143 (2021).
[31] P. Ranjan, T. K. Sahu, R. Bhushan, S. S. R. K. C. Yamijala, D. J. Late, P. Kumar, and A. Vinu, Freestanding borophene and its hybrids, Adv. Mater. **31**, 1900353 (2019).
[32] Y. Zhang, M. Yang, M. Zhou, S. Feng, W. Li, and J. Lin, A novel highly stable two-dimensional boron phase with promising potentials in energy fields, J. Mater. Chem. A **11**, 828 (2023).
[33] Y. Huang, S. N. Shirodkar, and B. I. Yakobson, Two-dimensional boron polymorphs for visible range plasmonics: A first-principles exploration, J. Am. Chem. Soc. **139**, 17181 (2017).
[34] G. Kresse and J. Hafner, Ab initio molecular dynamics for liquid metals, Phys. Rev. B **47**, 558 (1993).
[35] G. Kresse and J. Furthmüller, Efficiency of ab-initio total energy calculations for metals and semiconductors using a plane-wave basis set, Comput. Mater. Sci. **6**, 15 (1996).
[36] G. Kresse and J. Furthmüller, Efficient iterative schemes for ab initio total-energy calculations using a plane-wave basis set, Phys. Rev. B **54**, 11169 (1996).
[37] G. Kresse and J. Hafner, *Ab initio* molecular-dynamics simulation of the liquid-metal–amorphous-semiconductor transition in germanium, Phys. Rev. B **49**, 14251 (1994).
[38] G. Kresse and D. Joubert, From ultrasoft pseudopotentials to the projector augmented-wave method, Phys. Rev. B **59**, 1758 (1999).
[39] J. P. Perdew, K. Burke, and M. Ernzerhof, Generalized gradient approximation made simple, Phys. Rev. Lett. **77**, 3865 (1996).
[40] A. D. Becke and E. R. Johnson, A density-functional model of the dispersion interaction, J. Chem. Phys. **123**, 154101 (2005).
[41] S. Grimme, J. Antony, S. Ehrlich, and H. Krieg, A consistent and accurate *ab initio* parametrization of density functional dispersion correction (DFT-D) for the 94 elements H-Pu, J. Chem. Phys. **132**, 154104 (2010).
[42] S. Grimme, S. Ehrlich, and L. Goerigk, Effect of the damping function in dispersion corrected density functional theory, J. Comput. Chem. **32**, 1456 (2011).
[43] See Supplemental Material at http://link.aps.org/supplemental/10.1103/b2q9-fytt for convergence tests, stability tests, electronic property results, and magnetic property results.
[44] H.-D. Saßnick and C. Cocchi, Electronic structure of cesium-based photocathode materials from density functional theory: Performance of PBE, SCAN, and HSE06 functionals, Electron. Struct. **3**, 027001 (2021).
[45] J. Heyd, G. E. Scuseria, and M. Ernzerhof, Hybrid functionals based on a screened Coulomb potential, J. Chem. Phys. **118**, 8207 (2003).
[46] A. V. Krukau, O. A. Vydrov, A. F. Izmaylov, and G. E. Scuseria, Influence of the exchange screening parameter on the performance of screened hybrid functionals, J. Chem. Phys. **125**, 224106 (2006).
[47] P. Giannozzi, S. Baroni, N. Bonini, M. Calandra, R. Car, C. Cavazzoni, D. Ceresoli, G. L. Chiarotti, M. Cococcioni, I. Dabo, *et al.*, Quantum ESPRESSO: A modular and open-source software project for quantumsimulations of materials, J. Phys.: Condens. Matter **21**, 395502 (2009).
[48] D. R. Hamann, Optimized norm-conserving Vanderbilt pseudopotentials, Phys. Rev. B **88**, 085117 (2013).
[49] M. Methfessel and A. T. Paxton, High-precision sampling for Brillouin-zone integration in metals, Phys. Rev. B **40**, 3616 (1989).
[50] S. Baroni, S. De Gironcoli, A. D. Corso, and P. Giannozzi, Phonons and related crystal properties from density-functional perturbation theory, Rev. Mod. Phys. **73**, 515 (2001).
[51] G. Pizzi, V. Vitale, R. Arita, S. Blügel, F. Freimuth, G. Géranton, M. Gibertini, D. Gresch, C. Johnson, T. Koretsune, *et al.*, Wannier90 as a community code: New features and applications, J. Phys.: Condens. Matter **32**, 165902 (2020).
[52] P. Giannozzi, O. Baseggio, P. Bonfà, D. Brunato, R. Car, I. Carnimeo, C. Cavazzoni, S. De Gironcoli, P. Delugas, F. F. Ruffino, *et al.*, Quantum ESPRESSO toward the exascale, J. Chem. Phys. **152**, 154105 (2020).
[53] P. Giannozzi, O. Andreussi, T. Brumme, O. Bunau, M. B. Nardelli, M. Calandra, R. Car, C. Cavazzoni, D. Ceresoli, M. Cococcioni, *et al.*, Advanced capabilities for materials modelling with Quantum ESPRESSO, J. Phys.: Condens. Matter **29**, 465901 (2017).
[54] E. R. Margine and F. Giustino, Anisotropic Migdal-Eliashberg theory using Wannier functions, Phys. Rev. B **87**, 024505 (2013).
[55] J. Bardeen and D. Pines, Electron-phonon interaction in metals, Phys. Rev. **99**, 1140 (1955).
[56] F. Giustino, Electron-phonon interactions from first principles, Rev. Mod. Phys. **89**, 015003 (2017).
[57] P. B. Allen and R. C. Dynes, Transition temperature of strong-coupled superconductors reanalyzed, Phys. Rev. B **12**, 905 (1975).
[58] Y. Zhao, C. Lian, S. Zeng, Z. Dai, S. Meng, and J. Ni, Two-gap and three-gap superconductivity in AlB 2-based films, Phys. Rev. B **100**, 094516 (2019).
[59] F. Wooten, *Optical Properties of Solids* (Academic Press, New York, 1972).
[60] M. Gajdoš, K. Hummer, G. Kresse, J. Furthmüller, and F. Bechstedt, Linear optical properties in the projector-augmented wave methodology, Phys. Rev. B **73**, 045112 (2006).
[61] J. Weng and S.-P. Gao, A honeycomb-like monolayer of HfO2 and the calculation of static dielectric constant eliminating the

effect of vacuum spacing, Phys. Chem. Chem. Phys. **20**, 26453 (2018).

[62] A. Laturia, M. L. Van de Put, and W. G. Vandenberghe, Dielectric properties of hexagonal boron nitride and transition metal dichalcogenides: From monolayer to bulk, npj 2D Mater. Appl. **2**, 6 (2018).

[63] G. Yang and S.-P. Gao, A method to restore the intrinsic dielectric functions of 2D materials in periodic calculations, Nanoscale **13**, 17057 (2021).

[64] P. Li, X. Ren, and L. He, First-principles calculations and model analysis of plasmon excitations in graphene and graphene/hBN heterostructure, Phys. Rev. B **96**, 165417 (2017).

[65] D. Y. Zubarev and A. I. Boldyrev, Developing paradigms of chemical bonding: Adaptive natural density partitioning, Phys. Chem. Chem. Phys. **10**, 5207 (2008).

[66] L. Niu, O. J Conquest, C. Verdi, and C. Stampfl, Electronic and optical properties of 2D heterostructure bilayers of graphene, borophene and 2D boron carbides from first principles, Nanomaterials **14**, 1659 (2024).

[67] D. Liu, A. G. Every, and D. Tománek, Continuum approach for long-wavelength acoustic phonons in quasi-two-dimensional structures, Phys. Rev. B **94**, 165432 (2016).

[68] M. B. P. Querne, J. M. Bracht, J. L. F. Da Silva, A. Janotti, and M. P. Lima, Crystal structure and electrical and optical properties of two-dimensional Group-IV monochalcogenides, Phys. Rev. B **108**, 085409 (2023).

[69] I. Pallikara, P. Kayastha, J. M. Skelton, and L. D. Whalley, The physical significance of imaginary phonon modes in crystals, Electron. Struct. **4**, 033002 (2022).

[70] A. B. Migdal, Interaction between electrons and lattice vibrations in a normal metal, Sov. Phys. JETP **34**, 996 (1958).

[71] F. Marsiglio, Eliashberg theory: A short review, Ann. Phys. (N.Y.) **417**, 168102 (2020).

[72] G. M. Eliashberg, Interactions between electrons and lattice vibrations in a superconductor, Sov. Phys. JETP **11**, 696 (1960).

[73] N. Saunders, S. Palchoudhury, J. Jakowski, and J. Huang, Structural, electronic, and optical-absorption properties of 2D Si thin films, MRS Commun. **14**, 1273 (2024).

[74] GitHub repository Photonico/o-B14 20241024 at https://github.com/Photonico/.